## 6.1. Introduction

Binary, ternary, and multinary oxide materials are widely used in capacitors, microwaves and electronic high- and low power frequency devices, information storage, a variety of sensors, and charge storage devices [**1**–**9**]. There is a strong need for low-cost materials with large dielectrics, low tan δ, and large breakdown voltage for high power applications. Oxide materials have also been used in several fields such as medicine, imaging, and energy, where they require high critical current density under the magnetic field and for which a high-temperature superconductor material is required [**10**–**12**]. Since an ultrahigh dielectric permittivity was described in a $CaCu_3Ti_4O_{12}$ (CCTO) ceramic [**13**], extensive effort has been devoted to designing and developing materials with giant dielectric value in numerous ceramics. CCTO has been referred to as a pioneering large dielectric material because of its very dielectric constant ($\varepsilon' \sim 10^3 - 10^6$) and has been thoroughly studied [**14**–**17**]. It has been also demonstrated that values are independent of frequency between the $10^2$ and $10^6$ Hz range. CCTO exhibits good temperature stability across a large range of temperatures from 100 to 600 K without ferroelectric phase transition, in contrast to other materials of this class including $BaTiO_3$-based dielectric ceramics [**18**–**20**]. These characteristics further demonstrates suitability for above mentioned applications [**21**–**23**]. The genesis of the enormous dielectric constant of the CCTO has been the subject of numerous models from intrinsic and extrinsic mechanisms in the last 10 years [**24**–**26**]. Various models were proposed for the large dielectric constant such as the surface barrier layer capacitor (SBLC) [**27**], internal barrier layer capacitor (IBLC) [**28**, **29**], small polaron hopping models [30], polaronic stacking fault defect model [**26**], and non-Ohmic sample-electrode contact model [**31**]. For a very long time, CCTO was thought to be an unusual material among the several oxides related to

perovskites that can be generally represented by the chemical formula $ACu_3Ti_4O_{12}$ [**32**]. $Bi_{2/3}Cu_3Ti_4O_{12}$ (BCTO) is one of the few numbers that show compositionally and isostructural CCTO-like oxides. BCTO has also shown giant dielectric permittivity. With a high percentage of A-site vacancies, BCTO is a fascinating material since it signifies a distinct class of CCTO-like oxides and may thus be different from other similar materials of this class. It has been demonstrated that the processing method, composition, and morphology have a significant influence on the dielectric and electrical characteristics of the ceramics [**33**]. The dielectric characteristics of BCTO produced using a conventional solid-state method have been the subject of only a few papers [**34**, **35**]. Traditional and advanced ceramics are synthesized using a solid-state technique that requires laborious effort, a long reaction time, and multiple intermediate grinding steps [**36**]. Yang et al. produced a series of high density BCTO through the solid-state method and observed the dielectric constant of ~$3.3 \times 10^5$ at 1 kHz [**37**]. Gautam et al. [**38**] synthesized BCTO by semi wet route and observed to be a large dielectric permittivity of ~ $2.9\times10^4$ at 323 K and 100 Hz but the tangent loss of this ceramic was very high (~10). Zhuang et al. prepared BCTO-CCTO composites, has good candidate for dual function varistor-capacitor applications because of its high non-linear and dielectric properties [**39**]. There are limited reports on impurity substitution or how different processing methods affect microstructural, dielectric and electrical properties of BCTO ceramic. Vishnu et al. synthesized Ni-doped BCTO by semi wet route and reported to be high dielectric constant and low dielectric loss [**40**]. Because of processing methods and cationic substitution, further in-depth investigations are required to comprehend the impact of metal ions on their dielectric and electrical properties. To the best of the authors' knowledge, no studies have been done on the synthesis of $Bi_{(2/3)-x}Dy_xCu_3Ti_4O_{12}$(x=0.05, 0.10, and 0.20), also denoted as BDCTO-0.05,

BDCTO-0.1, and BDCTO-0.2 respectively, utilizing low cost $TiO_2$ as a source material. The morphology, crystalline structure, dielectric properties, and complex impedance, were determined for the materials developed using semi-wet method for the synthesis and results are reported in this paper.

## 6.2. Experimental

The BDCTO-0.05, BDCTO-0.1, and BDCTO-0.2 precursor powders were obtained by semi wet route, and the bismuth nitrate $Bi(NO_3)_3.5H_2O$ (99%) Merck, India) copper acetate $Cu(CH_3COO)_2$. H2O (99%) Merck, India), titanium oxide $TiO_2$ (98.5%) Merck, India), $DyN_3O_9.xH_2O$ (99.9% India), and citric acid ($C_6H_8O_7$, (99.5%) Merck, India)) were obtained from the Merk India. The purity of the source materials is listed as supplied by the supplier. The starting materials were mixed in the stoichiometric ratio, and distilled water was used as the solvent in this work. The resulting solution was heated to evaporate the water for self-ignition at 353–363 K on a hotplate with a magnetic stirrer. After the removal of a lot of gases, a residual mass of precursor powders was obtained. Citric acid is used in the ignition step as an agent that acts as a fuel. The precursor powders were ground and calcined at 1073 K for 6 h in an electrical furnace, respectively. A hydraulic press was used to consolidate the calcined powder containing 2 wt% polyvinyl alcohol (PVA) into cylindrical pellets. The PVA binder was burned out by heating at 573 K for two hours. Finally, the BDCTO-0.05, BDCTO-0.1, and BDCTO-0.2 pellets were sintered in the air for 8 h hours at 1173 K.

An X-ray Diffractometer (Rigaku miniflex 600, Japan) using Cu-ka radiation was used to determine the crystalline structure of the sintered sample. A scanning electron microscope was used to look at the microstructures of the fractured surfaces ((ZEISS; model EVO18 research, Germany). The elemental analysis of the sintered ceramics of the above-

mentioned system was performed using an energy dispersive X-ray analyzer (Oxford Instrument, USA). The size of the particles was investigated using a transmission electron microscope (TEM, Technai G2 20 S-Twin). The samples were sonicated for two hours after being distributed in ethanol for TEM investigation. This suspension was spread over a copper grid that had been coated with carbon before drying for eight hours in the oven. Thermo Fisher Scientific K (Waltham, MA) in broad scan survey mode and high energy resolution with AlK was used for the XPS investigation (1486.6 eV). The FTIR spectra of sintered powder were characterized by ATR-FTIR (Bruker, ALPHA model) Spectrophotometer using KBr pellets in the frequency range 400–4000 $cm^{-1}$. Dielectric dispersion and complex impedance were measured using an LCR meter (PSM1735, NumetriQN4L, U.K.) within the frequency range of 100 Hz- 5 MHz and the temperature range of 309 to 509 K.

## 6.3. Results and Discussion

### 6.3.1. Microstructural studies

Figure **6.1** (a) displays the X-ray diffraction (XRD) pattern of the materials BDCTO-0.05, BDCTO-0.1, and BDCTO-0.2 sintered at 1173 K for 8 h. This pattern demonstrates the development of single-phased crystals without any sign of secondary phases. The diffraction peaks at $2\theta^o$ = 24.2, 29.6, 34.2, 38.5, 42.3, 45.9, 49.3, 61.4 and 72.2$^o$, respectively, correspond to (200), (211), (220), (310), (222), (321), (400), (422) and (440) planes. The pseudo-cubic structure is visible in the XRD patterns of these ceramics, which were perfectly indexed with the BCTO PDF standard (JCPDS card No. 46-0725)). For the pseudo-cubic structure, none of the primary diffraction peaks exhibit a splitting peak [**41]**. As a result, all ceramics have a single-phase cubic structure with the space group Im-3. The average crystallite sizes (D) of the

ceramics were also calculated using the line broadening method and the XRD data. The Scherrer equation was used to determine the crystallite size (D) of the ceramics [**42**–**44**].

$$D = \frac{k\lambda}{\beta \cos\theta} \qquad 6.1$$

where $\theta$ is the diffraction angle, $\beta$ is the full width at half maximum (FWHM) for calculating crystallite size, $\lambda$ is the X-ray wavelength and $k$ is a constant taken as 0.89. The average value of crystallite size of BDCTO-0.05, BDCTO-0.1, and BDCTO-0.2 ceramics were calculated and the values are 39.98 nm, 38.13 nm, and 35.07 nm respectively.

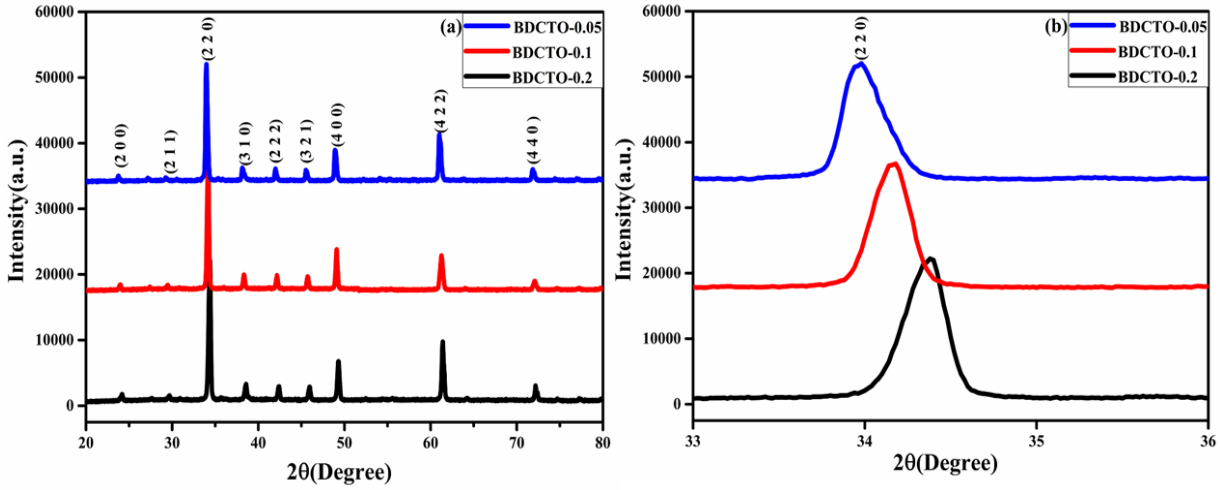


**Fig. 6.1** (a) XRD patterns for $Bi_{(2/3)-x}Dy_xCu_3Ti_4O_{12}$(x= 0.05, 0.10 and 0.20) ceramic ; (b) Inset figure of XRD patterns in the enlarged view at the range of 2θ from 31° to 33°.

The results of a Rietveld refinement analysis performed on the BDCTO-0.05, BDCTO-0.1, and BDCTO-0.2 sintered ceramics for XRD patterns are displayed in Figure **6.2** (a, b, c) respectively. The exact overlap of the predicted pattern (designated as a red circle) and the detected pattern (designated as a black circle) shows that the XRD patterns fit the data well [**45**–**47**]. The low value of $\chi^2$ further supported the accuracy of fitting for all samples. With the space group Im-3, all of the observed Bragg's peaks support the existence of cubic symmetry. Additionally, throughout the refinement process, variables relating to atomic locations, unit

cell parameters, half width parameters (U, V, and W), zero correction, background, atomic occupancy, and scale factor were varied. Table **6.1** also includes the refined values for the lattice parameter, angles, unit cell volume, FWHM parameters, Bragg R-factor, and RF-factor for all BDCTO-0.05, BDCTO-0.1, and BDCTO-0.2 ceramics. The (220) peak in inset figure **6.1** (b) shows a little peak displacement to a higher diffraction angle as the replacement concentration rises which is due to a smaller ionic radius of $Dy^{3+}$ than $Bi^{3+}$ ions[**48**]. The substituted cations effects on the lattice parameter have led to this little shift[**49**].

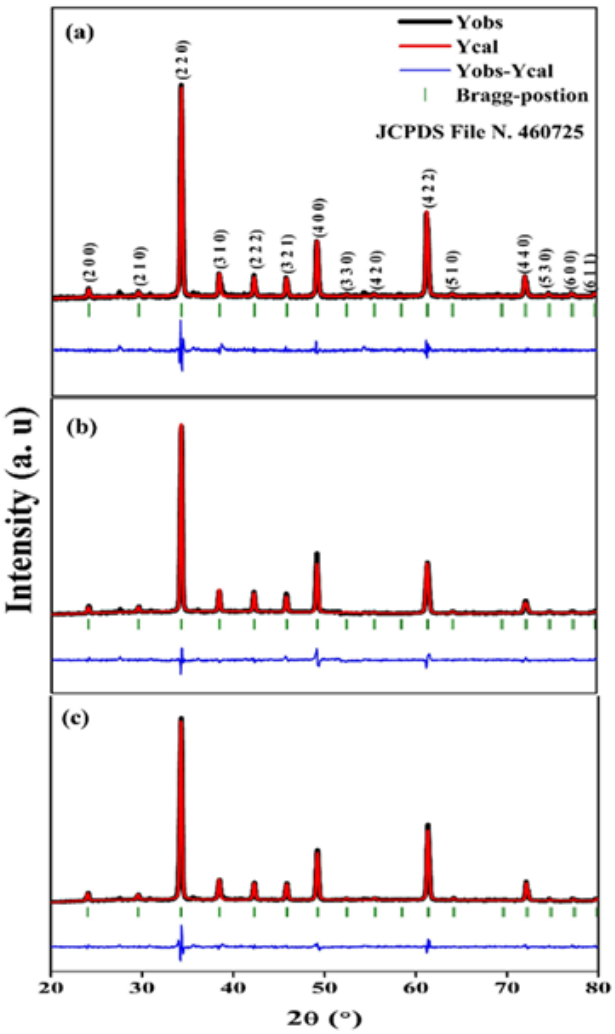


**Fig. 6.2** Rietveld refined XRD patterns of $Bi_{(2/3)-x}Dy_xCu_3Ti_4O_{12}$(x= 0.05, 0.10 and 0.20) ceramic sintered at 1173 K for 8 h.

**Table 6.1** Bragg R-factor, RF-factor lattice parameters, crystal structures, angles for $Bi_{(2/3)-x}Dy_xCu_3Ti_4O_{12}$ (x = 0.05, 0.10 and 0.20) ceramic.

| Samples | | Lattice parameters (Å) | $V_{cell}$ (Å$^3$) | FWHM Parameters | | | Bragg R-factor | RF -factor |
|---|---|---|---|---|---|---|---|---|
| BDCTO | $\chi^2$ | $a = b = c$ | | U | V | W | | |
| X = 0.05 | 4.08 | 7.404 | 405.834 | 0.07044 | -0.00447 | 0.068547 | 3.120 | 5.089 |
| X = 0.1 | 4.38 | 7.402 | 405.502 | 0.87713 | -0.65631 | 0.16754 | 2.771 | 2.174 |
| X= 0.2 | 3.77 | 7.401 | 405.456 | 0.00875 | -0.01849 | 0.06627 | 1.447 | 1.821 |
| Phase: $Bi_{(2/3)-x}Dy_xCu_3Ti_4O_{12}$ (BDCTO), Space group: lm-3, Angle: $\alpha = \beta = \gamma = 90°$, Cubic structure | | | | | | | | |

Figure **6.3** represents the bright field TEM image and SAED pattern of the BDCTO-0.05, BDCTO-0.1, and BDCTO-0.2 sintered ceramics. TEM images, as shown in Figure **6.3** (a-c) were used to determine the particle size and morphology of the above synthesized sintered ceramics. From the figure, we have observed that the particles are looking like spherical. Some of which showed some significantly agglomerated particles as well as individual particles in the images. The observed particle size of ceramics calculated by TEM images was found in the range of 96 ± 5 nm, 92 ± 5 nm, and 83 ± 5 nm respectively. The TEM images also show that the size of the particles in ceramics reduces as the $Dy^{3+}$ concentration rises. This indicates the beginning of lattice strain caused by an ionic size mismatch between $Dy^{3+}$ and $Bi^{3+}$, which speeds up particle nucleation and reduces particle growth [**51**, **52**]. The particle sizes determined by TEM and XRD observed the crystallite sizes were both in the nano-crystalline range. The polycrystalline nature of BDCTO-0.05, BDCTO-0.1, and BDCTO-0.2 ceramics was also verified by SAED patterns, shown in Figure **6.3** (d-f).

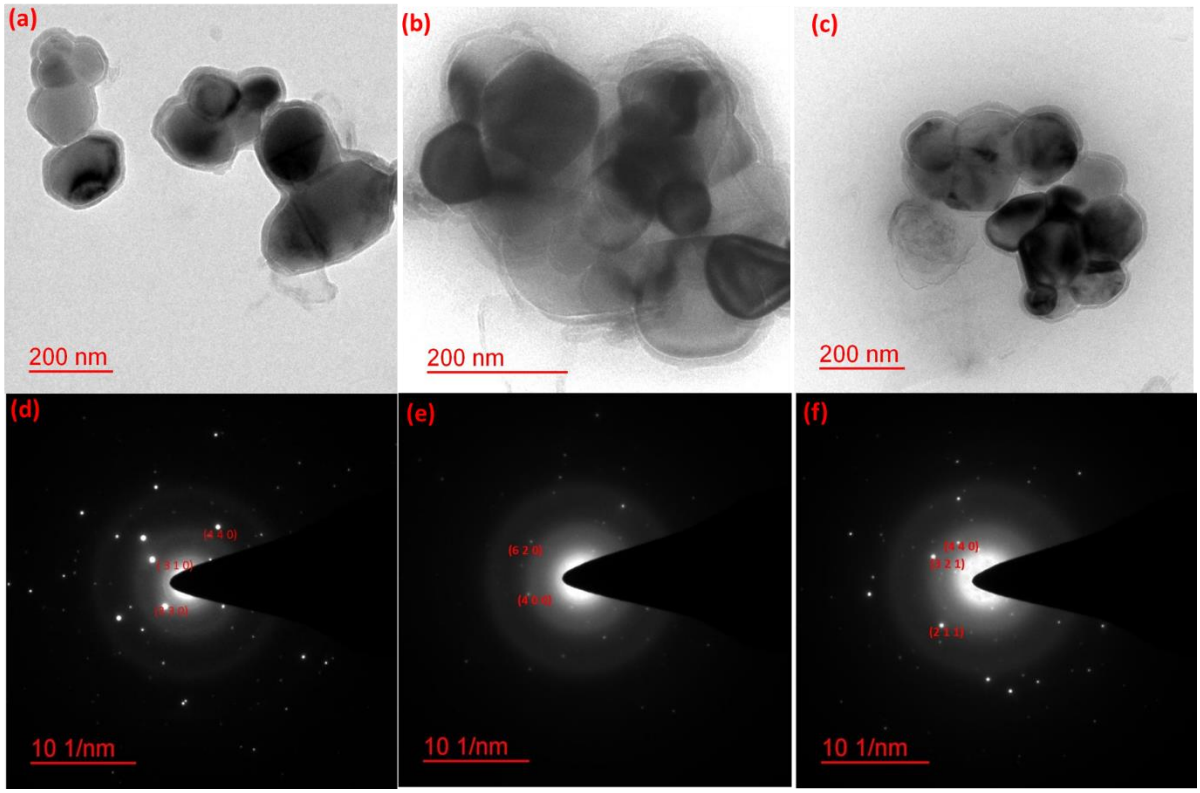


**Fig. 6.3** (a-c) Bright-field TEM image; (e-g) SAED pattern of $Bi_{(2/3)-x}Dy_xCu_3Ti_4O_{12}$(x= 0.05, 0.10 and 0.20) ceramic.

Figure **6.4** (a-c) represents the SEM image of the fractured surface and the corresponding grain size distribution of BDCTO-0.05, BDCTO-0.1, and BDCTO-0.2 sintered ceramics respectively. The graph reveals that the grains are well separated from each other as well as also bimodal distributed grain and compacted texture can be observed. It is evident from the SEM image that smaller grains were seen at the nanometer and larger grains at the micrometer range. The microstructure of BCTO ceramic is significantly impacted by Dy doping. The doped Dy content caused a considerably distinct behaviour in the microstructural progress. As shown in Figure, some holes appear on the surface of the ceramics, and their porosity decreases with increasing the Dy-doping content, It may be because Dy3+ addition has the effect of reducing oxygen vacancies since the migration of oxygen vacancies during the sintering process promotes grain development [**52**]. Inset figure **6.4** (a-c) represents the grain size

distribution curve for DCTO-0.05, BDCTO-0.1, and BDCTO-0.2 sintered ceramic respectively. It was observed from the figure that the grain size increases with rising the concentration which is due to the radius of the $Bi^{3+}$ ions being smaller than that of the $Dy^{3+}$ ions. The average grain sizes of the ceramics are 123.44 nm, 125.36 nm, and 132.11 nm, respectively. The increase in grain size of ceramic samples with Dy-doping may be one of the major factors leading to its dielectric properties and magnetic properties[**38**]. The EDX spectra of BDCTO-0.05, BDCTO-0.1, and BDCTO-0.2 sintered ceramics are shown in Figure **6.4** (d-f), which confirmed the existence of Bi, Dy, Cu, Ti, and O elements. Table 2 displays the atomic percentage of the elements Bi, Dy, Cu, Ti, and O with various compositions, verifying the purity and stoichiometry of ceramics.

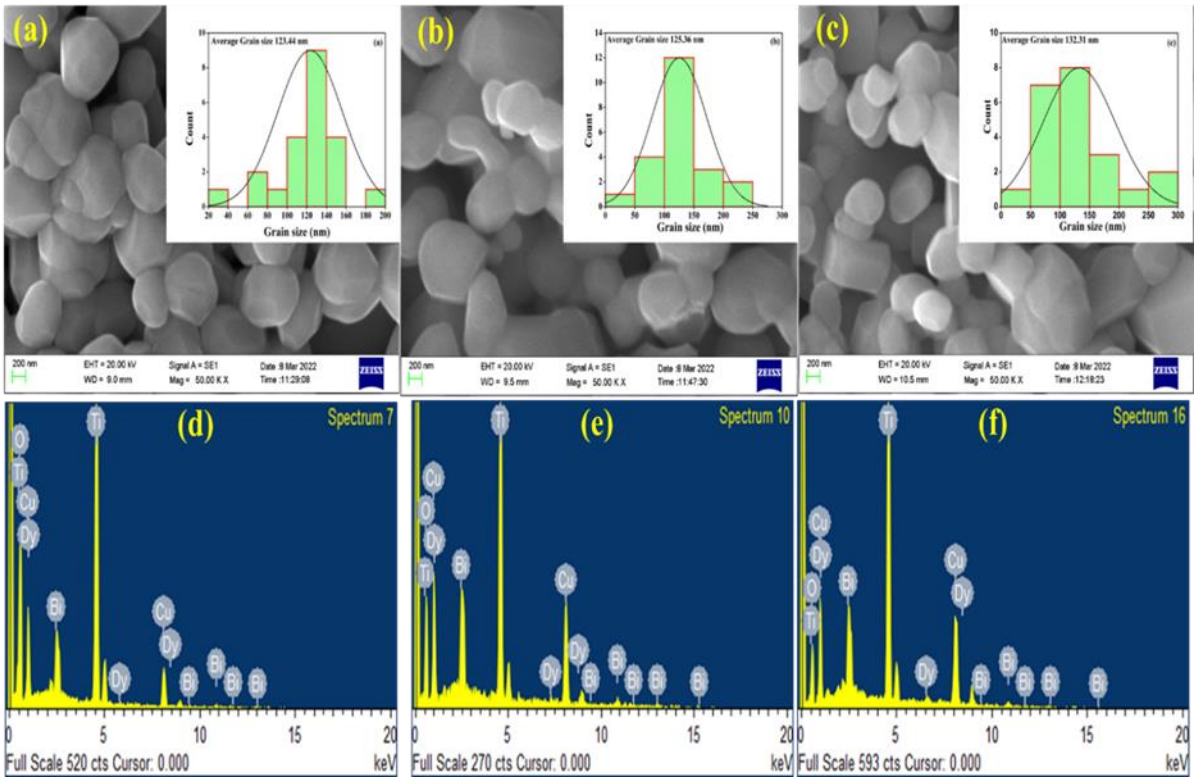


**Fig. 6.4** (a–c) SEM of sintered pellet; (e-g) EDX spectrum of $Bi_{(2/3)-x}Dy_xCu_3Ti_4O_{12}$(x= 0.05, 0.10 and 0.20) ceramic.

**Table 6.2** Atomic percentage of elements for $Bi_{(2/3)-x}Dy_xCu_3Ti_4O_{12}$ (x = 0.05, 0.10 and 0.20) sintered ceramic

| Composition | Atomic percent of element | | | | |
|---|---|---|---|---|---|
| | Bi | Dy | Cu | Ti | O |
| 0.05 | 2.40 | 0.17 | 11.68 | 15.57 | 70.18 |
| 0.10 | 2.72 | 0.45 | 14.40 | 19.20 | 63.23 |
| 0.20 | 2.48 | 0.92 | 15.97 | 21.29 | 59.34 |

The XPS method was used to ascertain the chemical states of the Bi, Dy, Cu, Ti, and O elements in the BDCTO-0.2 sintered ceramics. Figure **6.5 (a)** displays the obtained spectrum for Bi 4f. Approximately 158.58 eV and 163.86 eV, which correspond to Bi $4f_{7/2}$ and Bi $4f_{5/2}$, respectively, were the two typical peaks for Bi 4f, showing that bismuth was present in the ceramic as $Bi^{3+}$ [**40**]. The peak at 153.59 eV in Figure **6.5** (b) corresponds to the $Dy^{3+}$ ion in the $4d_{3/2}$ state at the 4d core level [53]. Figure **6.5** (c) shows the copper XPS spectra BDCTO-0.2 ceramic. With the binding energy associated with Cu 2p spectra at the peak 935.8 eV and 954.7 eV, which correspond to Cu $2p_{3/2}$ and Cu $2p_{1/2}$, respectively, the binding energy of copper in BDCTO-0.2 ceramic confirms the existence of the +2 oxidation state of Cu[**54**]. Figure **6.5** (d) displays the XPS spectrum of Ti 2p in BDCTO-0.2 sintered ceramic. The Ti 2p shown in the figure can be resolved into the contribution of $Ti^{3+}$ and $Ti^{4+}$ by fitting the spectrum which contains four peaks at the energies of 457.99 eV, 463.66 eV, 458.94 eV, and 465.97 eV respectively. The first two Peaks positions at 457.99 eV and 463.66 eV indicate the Ti 2p doublet i.e., Ti $2p_{3/2}$ and Ti $2p_{1/2}$, confirming the presence of Ti ions in the +4 oxidation state, and the later two peaks show the presence of Ti ions in the +3 oxidation state, which may be caused by the presence of oxygen vacancies during high-temperature sintering [**55**]. The three peaks at 529.49 eV, 530.84 eV, and 532.49 eV in the O 1s XPS spectrum (figure **6.5** (e)) can be attributed to oxygen-metal bonds, surface-adsorbed oxygen, and oxygen in the hydroxyl group respectively [**56**].

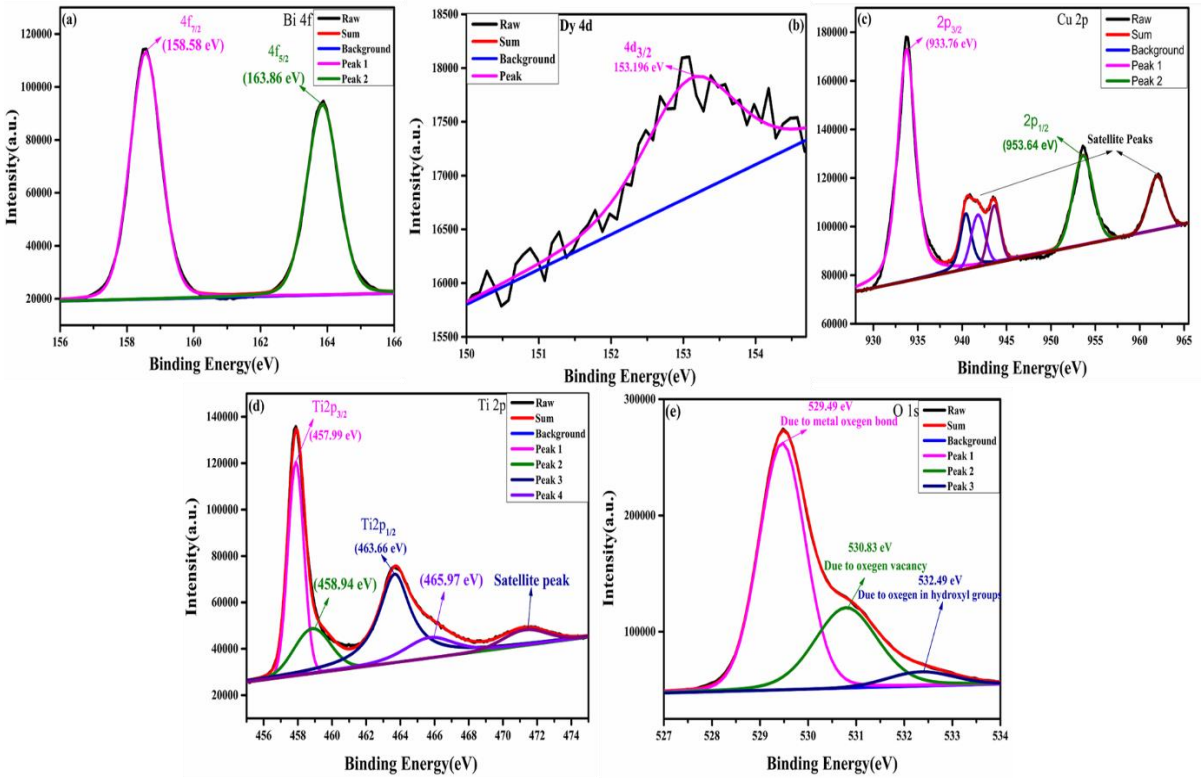


**Fig. 6.5** The XPS spectrum of (a) Bi; (b) Dy; (c) Cu; (d) Ti; (e) O elements present in the BDCTO-0.2 ceramics.

Figure **6.6** reveals the FTIR spectra of BDCTO-0.05, BDCTO-0.1, and BDCTO-0.2 ceramics sintered at 1173 K for 8 h and were recorded in the range of 400-4000 $cm^{-1}$. At 432 $cm^{-1}$, 505 $cm^{-1}$, and 595 $cm^{-1}$, the main characteristic bands of bismuth copper titanate ceramic were seen. The cause of these characteristic bands could be attributed to the region of $Ti^{4+}$ as a result of $\nu_{Ti-O}$ and $\nu_{Ti-O-Ti}$ vibrations [**57**, **58**]. The absorption peaks observed at 432 $cm^{-1}$ and 595 $cm^{-1}$ are mainly due to the $\nu_{Ti-O}$ stretching vibration, which signifies confirms the formation of the perovskite phase of bismuth copper titanate ceramic [**59**]. The peak recorded at 740 $cm^{-1}$ is mainly due to the presence of a metal oxide bond (Bi–O) [**60**, **61**]. According to the FTIR analysis, the absorption bands appear in the range of 300 $cm^{-1}$ to 700 $cm^{-1}$, which is caused by the mixed vibration of $CuO_4$ and $TiO_6$ octahedron [**36**]. The broad absorption bands at 1630

$cm^{-1}$ and 3440 $cm^{-1}$ could be related to the OH vibrational mode of the absorbed water molecule or moist atmosphere [**62**–**64**].

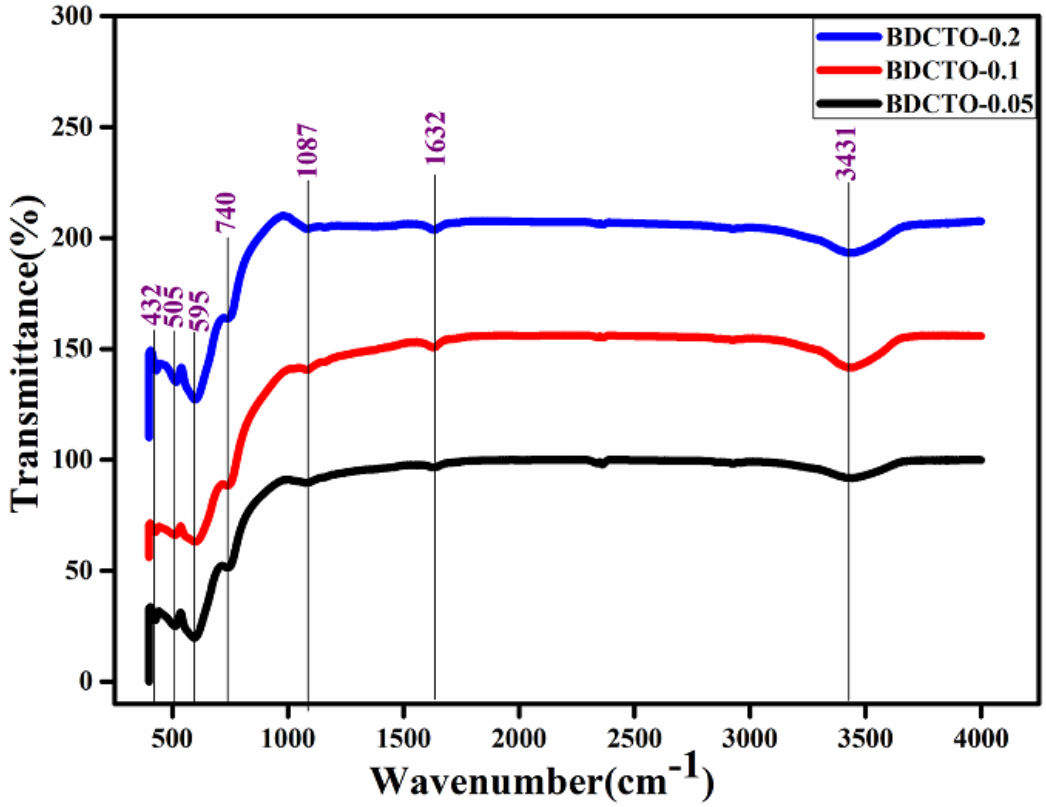


**Fig. 6.6** FTIR spectra of Dy doped BCTO system with various concentrations (x=0.05, 0.10 &0.20).

### 6.3.2. Dielectric studies

Figure **6.7** (a) illustrates the fluctuation of the dielectric constant ($\varepsilon_r$) as a function of frequency for the ceramics BDCTO-0.05, BDCTO-0.1, and BDCTO-0.2 respectively. Below 10 kHz, the dielectric constant of the ceramics falls off quickly, while between 10 kHz and 10 MHz, it virtually stays constant. As shown in the figure, the dielectric constant at 309 K is significantly higher for BDCTO-0.05 than for BDCTO-0.1 and BDCTO-0.2 ceramics. The values of $\varepsilon_r$ for the above ceramics at 309 K and 1 kHz were observed to be 285, 190, and 182 respectively. The occurrence of high dielectric constant at lower frequencies indicates the potential for

charge carriers to accumulate at the grain boundary and interface, leading to space charge polarization [**65**]. This explanation is based on the Maxwell-Wagner model, which states that dielectric materials with heterogeneous structures can be assumed to be made up of conducting grains and insulating grain boundaries. This situation results in the appearance of space charge polarization when the applied field drop crosses the grain boundaries[**66**]. It is also clear that the values $\varepsilon'$decrease as the concentration of $Dy^{3+}$ is increased. All the samples show a definite drop in the values of $\varepsilon'$as the frequency is increased evidently at a lower, intermediate, and higher frequency which is evident at lower, intermediate, and higher frequencies except pure BCTO ceramic(Synthesized by semi wet route) because it has observed frequency independent behaviour in higher frequency region and also reported literature [38, 67]. Tangent loss (tan δ) with frequency variation of the BDCTO-0.05, BDCTO-0.1, and BDCTO-0.2 sintered ceramics are shown in Figure **6.7** (b). The graph clearly shows that the value of tan δ drops with frequency in the lower frequency zone while decreasing smoothly in the higher frequency region. The value of tan δ of the above ceramics was found to be 0.61, 0.48, and 0.42 respectively, at 309 K and 1 kHz.

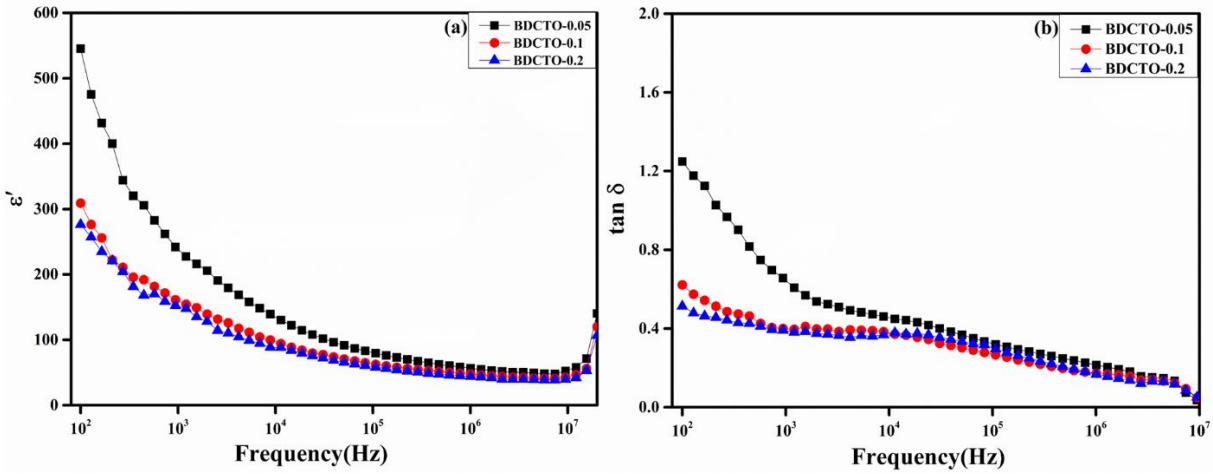


**Fig. 6.7** Frequency dependence of the (a) permittivity (ε′) and (b) dielectric loss (tan δ) for the Dy doped BCTO ceramics at 309 K and 1 kHz.

It is a useful method for evaluating the relation between the electrical properties of crystalline materials and their microstructures over a broad frequency and temperature range to reveal the cause of dielectric depression, the formation of the barrier layer, the presence of multiple polarization processes occurring simultaneously in the ceramics and their typical relaxation condition. The Nyquist plot between the real part of the impedance (Z′) and imaginary Part of impedance (Z″) of BDCTO-0.05, BDCTO-0.1, and BDCTO-0.2 sintered ceramics at 309 K is demonstrated in figure **6.8** (b). It is clear from the graph that only one semicircle is visible due to the contribution of the grain boundary while another semicircle is seen at a lower frequency region due to the electrode surface effect. This indicates that the material exhibits solid mixed ionic conductivity. There must be another semicircle in the high frequency region beyond the measurement frequency range since extrapolation in the high frequency region does not reveal the intercept on the Z′ axis (inset figure) to be near zero. This non-zero intercept obtained on the Z′ axis which does not pass through the origin gives the effective contribution of grains resistance ($R_g$) whereas the effective contribution of grain boundaries resistance ($R_{gb}$) is given by the intercept of another arc in the lower frequency range. The large value of grain boundary resistance which is typically seen for IBLC, a feature of semiconducting grain with insulating grain boundaries, suppresses the arc for grains at high frequency regions. From the figure, it can be seen that the values of grains and grain boundary resistance decrease with an increased doping concentration of $Dy^{3+}$. The calculated value of grains and grain boundaries resistance for BDCTO-0.05, BDCTO-0.1, and BDCTO-0.2 sintered ceramics were found to be 930 Ω, 465 Ω, 355 Ω, $4.33 \times 10^6$ Ω, $5.77 \times 10^6$ Ω and $6.78 \times 10^6$ Ω respectively.

Figure **6.8** (a) displays the variation of impedance (Z″) with frequency for BDCO-0.05, BDCTO-0.1, and BDCTO-0.2 sintered ceramics at 309 K. The figure shows that Z″ drops as

frequency rises and merges with itself at a higher frequency region. The relaxation peak seen at lower frequencies and suppression of peaks at higher frequency regions provides evidence for the existence of the thermally assisted ionic phenomenon in ceramics.

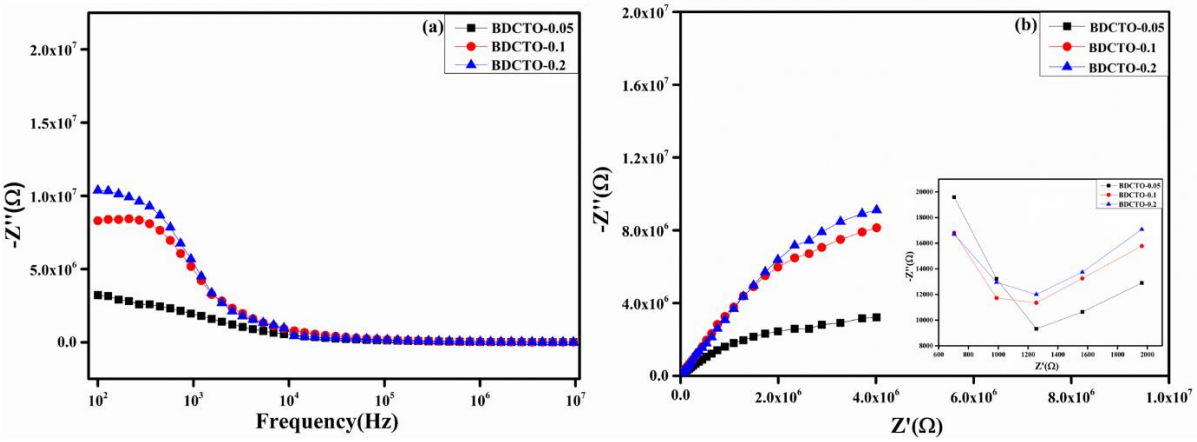


**Fig. 6.8** (a) Angular frequency-dependent Z″ plot and (b) complex impedance plot for BDCTO-0.05, BDCTO-0.1, and BDCTO-0.2 ceramics at 309 K.

Figure **6.9** (a) displays the plot of ln$\sigma_{ac}$ v/s 1000/T for BDCTO-0.05, BDCTO-0.1, and BDCTO-0.2 sintered ceramics. With temperature, the ac conductivity of all three samples rises practically linearly. As a result, at 1 kHz and in the 309 K- 500 K temperature range, the materials exhibit semiconductor characteristics. The activation energy of the samples having the composition (x =0.05, 0.10, and 0.20) are 0.454, 0.152, and 0.121 respectively. The activation energy linearly decreases with composition due to which charge carriers increase improving the conductivity of the produced materials [**68**, **69**]. Samples of BDCTO-0.05, BDCTO-0.1, and BDCTO-0.2 exhibit a rise in ac conductivity with rising dopant concentration.

Figure **6.9** (b) demonstrates the fluctuation of ac conductivity with frequency at 309 K for BDCTO-0.05, BDCTO-0.1, and BDCTO-0.2 sintered ceramics. It is clear from the figure that

ac conductivity increases with increasing frequency but in most materials, ac conductivity due to localized sites may be described by Jonscher's power law as revealed in the equation,

$$\sigma = \sigma_{dc}+\sigma_{ac} = \sigma_{dc}+ A\omega^{s} \quad 6.2$$

Where $\sigma_{dc}$ is direct current conductivity and *s* is the frequency exponent factor whose values lie between 0 to 1. The value of *s* also depends on the temperature as well as the composition. A is the pre-exponential factor and $\omega$ is the angular frequency. The value of *s* for BDCTO-0.05, BDCTO-0.1, and BDCTO-0.2 sintered ceramics was observed as 0.606, 0.654, and 0.731 respectively. From the results, it is concluded that the value of *s* increases with the rise in the $Dy^{3+}$ concentration and also observed that conductivity increases with increasing frequency which is a sign of the hopping conduction behavior of the ceramic[**70**,**71**].

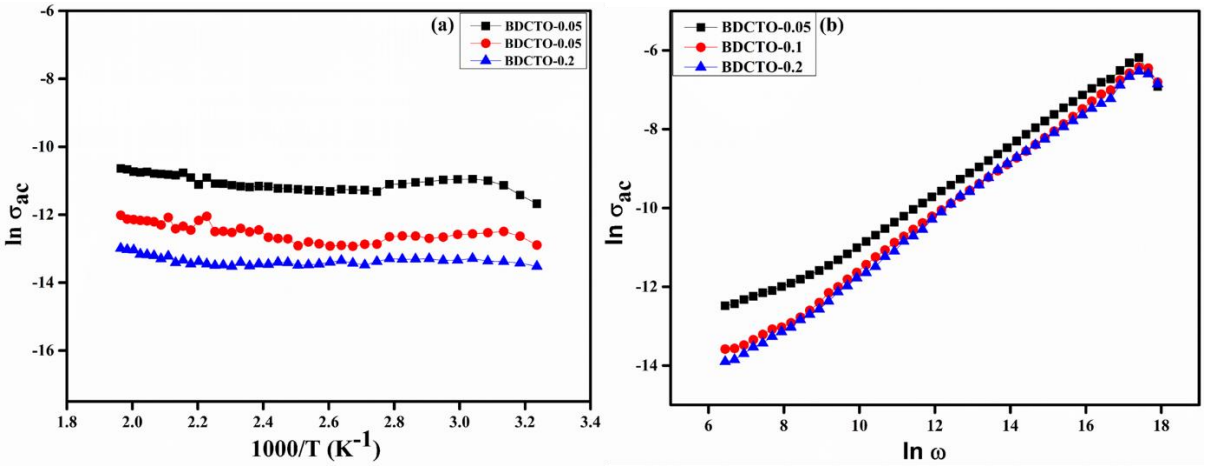


**Fig. 6.9** (a) Plots of conductivity (ln $\sigma_{ac}$) with the inverse of temperature at 1 kHz and (b) Variation of ln $\sigma_{ac}$ with ln $\omega$ at 309 K for $Bi_{(2/3)-x}Dy_xCu_3Ti_4O_{12}$(x= 0.05, 0.10 and 0.20) ceramic.

## 6.4. Conclusion

Dy-doped $Bi_{2/3}Cu_3Ti_4O_{12}$ was synthesized by semi wet route at 1173 K, and single-phase formation was confirmed by XRD studies without any sign of CuO and $TiO_2$ as a secondary phase. The lattice parameters of body centred BDCTO ceramic decrease due to lower ionic

radii of $Dy^{3+}$ than $Bi^{3+}$. The microstructure analysis exhibited that the grain growth of BCTO is largely affected by Dy-doping. The presence of each substituted and host element in the EDX spectra of BDCTO ceramics shows that the purity and stoichiometry of the ceramics are verified. The oxidation state of elements present in BDCTO ceramics was confirmed by XPS analysis. The frequency dependence of the dielectric investigation revealed that the dielectric constant and tangent loss fall as the Dy concentration rises in BCTO ceramic. The impedance investigations of BDCTO ceramics revealed an unusual grain boundary resistance, which confirms the IBLC mechanism existing in this ceramic and is responsible for the high $\varepsilon'$ values. ac conductivity studies are done as a function of both frequency and temperature. As the frequency increases, the ac conductivity increases following the Jonscher power law, and also rises with the temperature that obeys the Arrhenius law.

## 6.5. Reference

**[1]** G. R. Gajula, L. R. Buddiga, K. N. Chidambara Kumar, and M. Dasari, "Study on electric modulus, complex modulus and conductivity properties of Nb/Sm, Gd doped barium titanate-lithium ferrite ceramic composites," Results in Physics, **17** (2020) 103076.

**[2]** Y. Wang, W. Jie, C. Yang, X. Wei, and J. Hao, "Colossal permittivity materials as superior dielectrics for diverse applications," Advanced Functional Materials, **29** (2019) 1808118.

**[3]** N. G. Imam, M. AbouHasswa, and N. Okasha, "Synchrotron X-ray absorption fine structure study and dielectric performance of $Li_{0.5}Fe_{2.5}O_4/BaTiO_3$ multiferroic," Journal of Materials Science: Materials in Electronics, 32 (2021) 21492-21510.

**[4]** Y. Slimani, A. Selmi, E. Hannachi, M. A. Almessiere, A. Baykal, I. Ercan, "Impact of ZnO addition on structural, morphological, optical, dielectric and electrical performances of $BaTiO_3$ ceramics," Journal of Materials Science: Materials in Electronics, **30** (2019) 9520-9530.

**[5]** M. A. Almessiere, Y. Slimani, H. S. El Sayed, A. Baykal, I. Ercan, "Microstructural and magnetic investigation of vanadium-substituted Sr-nanohexaferrite," Journal of Magnetism and Magnetic Materials, **471** (2019) 124-132.

**[6]** M. A. Almessiere, Y. Slimani, M. Sertkol, M. Nawaz, A. Sadaqat, A. Baykal, I. Ercan, B. Ozçelik, "Effect of $Nb^{3+}$ substitution on the structural, magnetic, and optical properties of $Co_{0.5}Ni_{0.5}Fe_2O_4$ nanoparticles," Nanomaterials, **9** (2019) 430.

**[7]** A. Manikandan, M. Yogasundari, K. Thanrasu, A. Dinesh, K. K. Raja, Y. Slimani, S. K. Jaganathan, R. Srinivasan, A. Baykal, "Structural, morphological and optical

properties of multifunctional magnetic-luminescent ZnO@$Fe_3O_4$ nanocomposite," Physica E: Low-dimensional Systems and Nanostructures, 124 (2020) 114291.

**[8]** A. S. Hassanien, H. R. Alamri, I. M. El Radaf, "Impact of film thickness on optical properties and optoelectrical parameters of novel $CuGaGeSe_4$ thin films synthesized by electron beam deposition," Optical and Quantum Electronics, **52** (2020) 335.

**[9]** A. S. Hassanien, I. Sharma, "Dielectric properties, Optoelectrical parameters and electronic polarizability of thermally evaporated a-Pb-Se-Ge thin films," Physica B: Condensed Matter, **622** (2021) 413330.

**[10]** A. Hamrita, Y. Slimani, M. K. Ben Salem, E. Hannachi, L. Bessais, F. Ben Azzouz, M. Ben Salem, "Superconducting properties of polycrystalline $YBa_2Cu_3O_{7-d}$ prepared by sintering of ball-milled precursor powder," Ceramics International, **40** (2014) 1461-1470.

**[11]** Y. Slimani, E. Hannachi, M. K. Ben Salem, A. Hamrita, M. Ben Salem, F. Ben Azzouz, "Excess conductivity study in nano-$CoFe_2O_4$-Added $YBa_2Cu_3O_{7-d}$ and $Y_3Ba_5Cu_8O_{18\pm x}$ superconductors," Journal of Superconductivity and Novel Magnetism, **28** (2015) 3001-3010.

**[12]** M. K. Ben Salem, E. Hannachi, Y. Slimani, A. Hamrita, M. Zouaoui, L. Bessais, M. Ben Salem, F. Ben Azzouz, "$SiO_2$ nanoparticles addition effect on microstructure and pinning properties in $YBa_2Cu_3O_y$," Ceramics International, **40** (2014) 4953-4962.

**[13]** P. Cheng, D. Wang, Z. Dang, Q. Luo, M. Zhou, "Influence of donor doping on dielectric properties of calcium copper titanate ceramics." AIP Advances, **12** (2022).

**[14]** R. Wu, M. Ma, S. Zhang, P. Zhao, K. Li, Q. Zhao, A. Chang, B. Zhang, "Enhanced linearity of $CaCu_3Ti_4O_{12}$ by changing energy band structure induced by $Fe^{3+}$ doping for

high temperature thermistor application," Applied Physics Letters, **121** (2022).

**[15]** Z. Zhang, S. Shu, Z. Wang, Z. Xie, H. Wang, C. Li, S. Ke, L. Shu, "The flexoelectric transition in $CaCu_3Ti_4O_{12}$ material with colossal permittivity," Journal of Applied Physics, **132** (2022).

**[16]** J. Zhang, J. Zheng, Y. Li, Y. Liu, W. Hao, L. Lin, Y. Li, J. Song, "Effect of different pH values adjusted by ammonia on the dielectric properties of $CaCu_3Ti_4O_{12}$ ceramics prepared by a sol-gel method," Journal of Alloys and Compounds, **779** (2019) 255-260.

**[17]** Y. Guo, J. Tan, J. Zhao, "Influence of CTO additives on microstructure and electrical properties of CCTO ceramics," Materials Chemistry and Physics, **278** (2022) 125659.

**[18]** S. G. Infantiya, A. Aslinjensipriya, R. S. Reena, S. Deepapriya, J. D. Rodney, S. J. Das, C. J. Raj, "Calcium copper titanate a perovskite oxide structure: effect of fabrication techniques and doping on electrical properties—a review," Journal of Materials Science: Materials in Electronics, **33** (2022) 15992-16028.

**[19]** L. Liu, S. Ren, J. Liu, F. Han, J. Zhang, B. Peng, D. Wang, A. A. Bokov, Z.-G. Ye, "Localized polarons and conductive charge carriers: understanding $CaCu_3Ti_4O_{12}$ over a broad temperature range," Physical Review B, **99** (2019) 094110.

**[20]** M.B. Smith, K. Page, T. Siegrist, P. L. Redmond, E. C. Walter, R. Seshadri, L. E. Brus, M. L. Steigerwald, "Crystal structure and the paraelectric-to-ferroelectric phase transition of nanoscale $BaTiO_3$," Journal of the American Chemical Society, **130** (2008) 6955-6963.

**[21]** P. Mao, J. Wang, S. Liu, L. Zhang, Y. Zhao, L. He, "Grain size effect on the dielectric and non-ohmic properties of $CaCu_3Ti_4O_{12}$ ceramics prepared by the sol-gel process," Journal of Alloys and Compounds, **778** (2019) 625-632.

**[22]** R. K. Pandey, W. A. Stapleton, J. Tate, A. K. Bandyopadhyay, I. Sutanto, S. Sprissler, S. Lin, AIP Adv, **3** 62126 (2013).

**[23]** S. Rani, N. Ahlawat, K. M. Sangwan, S. Rani, R. Punia, J. Malik, "Structural investigation and giant dielectric response of $CaCu_3Ti_4O_{12}$ ceramic by Nd/Zr co-doping for energy storage applications," Journal of Materials Science: Materials in Electronics, **29** (2018) 10825-10833.

**[24]** P. Mandal and A. Sundaresan, "Dielectric relaxation mechanism in high-pressure synthesized $BiCr_{0.5}Mn_{0.5}O_3$," Journal of Electronic Materials, **50** (2021) 1615-1620.

**[25]** W. Hao, B. Yu, P. Xu, L. Sun, E. Cao, Y. Zhang, "Reducing the low-frequency dielectric loss of $CaCu_3Ti_4O_{12}$ ceramics by adding $(In_{0.5}Nb_{0.5})_{0.05}Ti_{0.95}O_2$," Journal of Materials Science: Materials in Electronics, **32** (2021) 9324-9331.

**[26]** P. R. Bueno, R. Tararan, R. Parra, E. Joanni, M. A. Ramírez, W. C. Ribeiro, E. Longo, J. A. Varela, "A polaronic stacking fault defect model for $CaCu_3Ti_4O_{12}$ material: an approach for the origin of the huge dielectric constant and semiconducting coexistent features," Journal of Physics D: Applied Physics, **42** (2009) 055404.

**[27]** W. Dong, W. Hu, A. Berlie, K. Lau, H. Chen, R. L. Withers, Y. Liu, "Colossal dielectric behavior of Ga+Nb co-doped rutile $TiO_2$," ACS applied materials & interfaces, **7** (2015) 25321-25325.

**[28]** R. Schmidt, M. C. Stennett, N. C. Hyatt, J. Pokorny, J. Prado-Gonjal, M. Li, D. C. Sinclair, "Effects of sintering temperature on the internal barrier layer capacitor (IBLC) structure in $CaCu_3Ti_4O_{12}$ (CCTO) ceramics," Journal of the European Ceramic Society, **32** (2012) 3313-3323.

**[29]** Y. Song, X. Wang, X. Zhang, Y. Sui, Y. Zhang, Z. Liu, Z. Lv, Y. Wang, P. Xu, B.

Song, "The contribution of doped-Al to the colossal permittivity properties of $Al_xNb_{0.03}Ti_{0.97-x}O_2$ rutile ceramics," Journal of Materials Chemistry C, **4** (2016) 6798-6805.

**[30]** K. Meeporn, N. Chanlek, P. Thongbai, "Effects of DC bias on non-ohmic sample-electrode contact and grain boundary responses in giant-permittivity $La_{1.7}Sr_{0.3}Ni_{1-x}Mg_xO_4$ ceramics," RSC Advances, **6** (2016) 91377-91385.

**[31]** T. Nachaithong, P. Thongbai, S. Maensiri, "Colossal permittivity in $(In_{1/2}Nb_{1/2})_xTi_{1-x}O_2$ ceramics prepared by a glycine nitrate process," Journal of the European Ceramic Society, **37** (2017) 655-660.

**[32]** K. Pal, R. Jana, A. Dey, P. P. Ray, M. M. Seikh, A. Gayen, "Performance analysis of Fe-doped calcium copper titanate quadruple perovskite in optoelectronic device," Chemical Physics Letters, 709 (2018) 110-115.

**[33]** Y. Slimani, A. Selmi, E. Hannachi, M. A. Almessiere, G. AlFalah, L. F. AlOusi, G. Yasin, M. Iqbal, "Study on the addition of $SiO_2$ nanowires to $BaTiO_3$: Structure, morphology, electrical and dielectric properties," Journal of Physics and Chemistry of Solids, **156** (2021) 110183.

**[34]** M. M. Ahmad, A. Alshoaibi, S. A. Ansari, T. S. Kayed, H. A. Khater, H. M. Kotb, "Dielectric properties of $Bi_{2/3}Cu_3Ti_4O_{12}$ ceramics prepared by mechanical ball milling and low temperature conventional sintering," Materials, **15** (2022) 3173.

**[35]** S. Mustapha, J. O. Tijani, M. M. Ndamitso, A. S. Abdulkareem, D. T. Shuaib, A. T. Amigun, H. L. Abubakar, "Facile synthesis and characterization of $TiO_2$ nanoparticles: X-ray peak profile analysis using Williamson–Hall and Debye–Scherrer methods," International Nano Letters, **11** (2021) 241-261.

**[36]** L. Singh, I. W. Kim, B. C. Sin, K. D. Mandal, U. S. Rai, A. Ullah, H. Chung, Y. Lee, "Dielectric studies of a nano-crystalline $CaCu_{2.90}Zn_{0.10}Ti_4O_{12}$ electro-ceramic by one pot glycine assisted synthesis from inexpensive $TiO_2$ for energy storage capacitors," RSC Advances, **4** (2014) 52770-52784.

**[37]** L. Yang, G. Huang, T. Wang, H. Hao, Y. Tian, "Colossal dielectric permittivity and relevant mechanism of $Bi_{2/3}Cu_3Ti_4O_{12}$ ceramics," Ceramics International **42** (2016) 9935-9939.

**[38]** P. Gautam, A. Khare, S. Sharma, N. B. Singh, K. D. Mandal, "Characterization of $Bi_{2/3}Cu_3Ti_4O_{12}$ ceramics synthesized by semi-wet route," Progress in Natural Science: Materials International, **26** (2016) 567-571.

**[39]** Z. Tang, K. Wu, J. Li, S. Huang, "Optimized dual-function varistor-capacitor ceramics of core-shell structured $xBi_{2/3}Cu_3Ti_4O_{12}$ /$(1-x)CaCu_3Ti_4O_{12}$ composites," Journal of the European Ceramic Society, **40** (2020) 3437-3444.

**[40]** V. S. Rai, D. Prajapati, V. Kumar, M. K. Verma, S. Pandey, T. Das, N. B. Singh, K. D. Mandal, "Low temperature synthesis, dielectric and electrical characteristics of $Bi_{2/3}Cu_{3-x}Ni_xTi_4O_{12}$ (where x= 0.05, 0.1, and 0.2) ceramics for the dielectric and electrical properties," Journal of Materials Science: Materials in Electronics, **33** (2022) 5273-5282.

**[41]** A. A. Akl, I. M. El Radaf, A. S. Hassanien, "An extensive comparative study for microstructural properties and crystal imperfections of Novel sprayed $Cu_3SbSe_3$ Nanoparticle-thin films of different thicknesses," Optik, **227** (2021) 165837.

**[42]** A. K. Rai, K. D. Mandal, D. Kumar, O. Parkash, "Characterization of nickel doped CCTO: $CaCu_{2.9}Ni_{0.1}Ti_4O_{12}$ and $CaCu_3Ti_{3.9}Ni_{0.1}O_{12}$ synthesized by semi-wet

route," Journal of alloys and compounds, **491** (2010) 507-512.

**[43]** Y. Slimani, B. Unal, M. A. Almessiere, E. Hannachi, G. Yasin, A. Baykal, I. Ercan, "Role of $WO_3$ nanoparticles in electrical and dielectric properties of $BaTiO_3$–$SrTiO_3$ ceramics," Journal of Materials Science: Materials in Electronics, **31** (2020) 7786-7797.

**[44]** Y. Slimani, B. Unal, M. A. Almessiere, A. D. Korkmaz, S. E. Shirsath, G. Yasin, A. V Trukhanov, A. Baykal, "Investigation of structural and physical properties of Eu3+ ions substituted $Ni_{0.4}Cu_{0.2}Zn_{0.4}Fe_2O_4$ spinel ferrite nanoparticles prepared via sonochemical approach," Results in Physics, **17** (2020) 103061.

**[45]** L. Singh, I. W. Kim, B. C. Sin, S. K. Woo, S. H. Hyun, K. D. Mandal, Y. Lee, "Combustion synthesis of nano-crystalline $Bi_{2/3}Cu_3Ti_{2.90}Fe_{0.10}O_{12}$ using inexpensive $TiO_2$ raw material and its dielectric characterization," Powder technology, **280** (2015) 256-265.

**[46]** T. Tchouank Tekou Carol, J. Sharma, J. Mohammed, S. Kumar, and A. K. Srivastava "Effect of temperature on the magnetic properties of nano-sized M-type barium hexagonal ferrites." AIP Conference Proceedings, **1860** (2017).

**[47]** E. Hannachi, K. A. Mahmoud, M. I. Sayyed, Y. Slimani, "Structure, optical properties, and ionizing radiation shielding performance using Monte Carlo simulation for lead-free BTO perovskite ceramics doped with ZnO, $SiO_2$, and $WO_3$ oxides," Materials Science in Semiconductor Processing, **145** (2022) 106629.

**[48]** X. Huang, H. Zhang, M. Wei, Y. Lai, and J. Li, "Effect of semiconductive grain and microstructure on the dielectric properties of $CaCu_3Ti_4O_{12}$ ceramics with $Sr^{2+}$ doping," Journal of Alloys and Compounds, **708** (2017) 1026-1032.

**[49]** Z. K. Heiba, M. B. Mohamed, A. M. Wahba, N. G. Imam, "Structural, optical, and electronic characterization of Fe-doped alumina nanoparticles," Journal of Electronic Materials, **47** (2018) 711-720.

**[50]** V. S. Rai, S. Pandey, V. Kumar, M. K. Verma, A. Kumar, S. Singh, D. Prajapati, K. D. Mandal, "Investigation of microstructure and dielectric behavior of $Bi_{2/3}Cu_{3-x}Mg_xTi_4O_{12}$ (x= 0, 0.05, 0.1 and 0.2) ceramics synthesized by semi-wet route," Journal of Materials Science: Materials in Electronics, **32** (2021) 7671-7680.

**[51]** S. Chauhan, M. Kumar, S. Chhoker, S. C. Katyal, M. Singh, "Substitution driven structural and magnetic transformation in Ca-doped BiFeO 3 nanoparticles," RSC advances, **6** (2016) 43080-43090.

**[52]** G. Hussain, F. Rehman, I. Ahmed, Y. Jamil, H. Anwar, "Synthesis, characterization and machine learning assisted optical emission studies of dysprosium doped bismuth ferrites," Materials Research Bulletin,**160** (2023) 112108.

**[53]** M. Venugopal, H. P. Kumar, and R. Jayakrishnan, "Tunable blue-yellow and orange-red emissions from Dysprosium and Samarium doped $SrCeO_3$ perovskite systems," Journal of Solid State Chemistry, **296** (2021) 121975.

**[54]** V. Kumar, A. Kumar, M. K. Verma, S. Singh, S. Pandey, V. S. Rai, D. Prajapati, T. Das, N. B. Singh, K. D. Mandal, "Investigation of dielectric and electrochemical behavior of $CaCu_{3-x}Mn_xTi_4O_{12}$ (x= 0, 1) ceramic synthesized through semi-wet route," Materials Chemistry and Physics, **245** (2020) 122804.

**[55]** S. Kawrani, M. Boulos, M. F. Bekheet, R. Viter, A. A. Nada, W. Riedel, S. Roualdes, D. Cornu, M. Bechelany, "Segregation of copper oxide on calcium copper titanate surface induced by Graphene Oxide for Water splitting applications," Applied Surface

Science, **516** (2020) 146051.

**[56]** N. Li, M. Shi, Y. Xin, W. Zhang, J. Qin, K. Zhang, H. Lv, M. Yuan, C. Wang, "Oxygen vacancies-modified S-scheme $Bi_2Ti_2O_7/CaTiO_3$ heterojunction for highly efficient photocatalytic NO removal under visible light," Journal of Environmental Chemical Engineering, **10** (2022) 107420.

**[57]** P. Thiruramanathan, A. Marikani, T. Vigneswari, R. Srinivasan, K. Jeyapappa, "Investigating the Dielectric and Ferroelectric Properties of $(Bi_4Ti_3O_{12})_{0.4}$–$(CaCu_3Ti_4O_{12})_{0.6}$ Nanocomposite Ceramics, Thin Films and Thick Films for Microwave and Microelectronic Applications," Journal of Alloys and Compounds, (2024) 174668.

**[58]** S. Sharma, T. Tekou Carol T, J. Mohammed, D. Basandrai, A. K. Srivastava, "Structural, magnetic, and optical study of $La^{3+}$-$Co^{2+}$-substituted Ni2Y-type barium hexaferrites," Journal of Materials Research, **38** (2023) 2156-2168.

**[59]** R. Sankar Ganesh, S. K. Sharma, N. Abinnas, E. Durgadevi, P. Raji, S. Ponnusamy, C. Muthamizhchelvan, Y. Hayakawa, D. Y. Kim, "Fabrication of the flexible nanogenerator from BTO nanopowders on graphene coated PMMA substrates by sol-gel method," Materials Chemistry and Physics, **192** (2017) 274-281.

**[60]** V. S. Rai, D. Prajapati, M. K. Verma, V. Kumar, S. Pandey, T. Das, N. B. Singh, K. D. Mandal, "Influence of Zn doping on microstructure, dielectric, and electric properties in $Bi_{2/3}Cu_3Ti_4O_{12}$ ceramic synthesized by the semi-wet method," Journal of Materials Science: Materials in Electronics, **33** (2022) 14868-14881.

**[61]** M. H. A. Mhareb, Y. Slimani, Y. S. Alajerami, M. I. Sayyed, E. Lacomme, M. A. Almessiere, "Structural and radiation shielding properties of $BaTiO_3$ ceramic with

different concentrations of Bismuth and Ytterbium," Ceramics International **46** (2020) 28877-28886.

**[62]** P. Thomas, A. Ashokbabu, R. Vaish, "Structural, thermal and dielectric properties and thermal degradation kinetics of nylon11/$CaCu_3Ti_4O_{12}$(CCTO) nanocomposites," Journal of Thermal Analysis and Calorimetry, 141 (2020) 1123-1135.

**[63]** M. A. Ahmed, N. Okasha, N. G. Imam, "Crossover between PEG and BT/NZF magnetoelectric nanocomposites for tailoring applicable multiferroic materials," Journal of Superconductivity and Novel Magnetism, **28** (2015) 2783-2793.

**[64]** M. A. Ahmed, N. Okasha, N. G. Imam, "Advanced imaging techniques for characterization of $0.5BaTiO_3/0.5Ni_{0.5}Zn_{0.5}Fe_2O_4$ multiferroic nanocomposite," Journal of alloys and compounds, 557 (2013) 130-141.

**[65]** S. Jesurani, S. Kanagesan, R. Velmurugan, T. Kalaivani, "Phase formation and high dielectric constant of calcium copper titanate using sol–gel route," Journal of Materials Science: Materials in Electronics, **23** (2012) 668-674.

**[66]** T. T. Carol T, J. Mohammed, R. Bhargava, S. Khan, S. Mishra, S. K. Godara, A. K. Srivastava, "Crystal structure refinement, optical properties, dielectric response, and impedance spectroscopy of $Ni^{2+}$-$Co^{2+}$ substituted bismuth copper titanate (BCTO)," Materials Chemistry and Physics, **248** (2020) 122933.

**[67]** S. Pandey, A. Kumar, N. B. Singh, K. D. Mandal, "Studies on dielectric and magnetic properties of $CaCu_3Ti_3MnO_{12}$ ceramic synthesized via semi-wet route." Journal of the Australian Ceramic Society **56** (2020) 915-922.

**[68]** A. Kumar, M. K. Verma, S. Singh, T. Das, L. Singh, K. D. Mandal, "Electrical, magnetic and dielectric properties of cobalt-doped barium hexaferrite

$BaFe_{12-x}Co_xO_{19}$(x= 0.0, 0.05, 0.1 and 0.2) ceramic prepared via a chemical route," Journal of Electronic Materials, **49** (2020) 6436-6447.

**[69]** N. Y. Mostafa, M. B. Mohamed, N. G. Imam, M. Alhamyani, Z. K. Heiba, "Electrical and optical properties of hydrogen titanate nanotube/PANI hybrid nanocomposites," Colloid and Polymer Science, **294** (2016) 215-224.

**[70]** Y. Ben Taher, A. Oueslati, N. K. Maaloul, K. Khirouni, M. Gargouri, "Conductivity study and correlated barrier hopping (CBH) conduction mechanism in diphosphate compound," Applied Physics A, **120** (2015) 1537-1543.

**[71]** M. A. Ahmed, N. Okasha, N. G. Imam, "Modification of composite ceramics properties via different preparation techniques," Journal of magnetism and magnetic materials, **324** (2012) 4136-4142.